Journal of Alloys and Compounds 706 (2017) 461–469

Contents lists available at ScienceDirect

Journal of Alloys and Compounds

journal homepage: http://www.elsevier.com/locate/jalcom

Different morphologies of ZnO and their triethylamine sensing properties

Wenru Li, Hongyan Xu*, Huanqin Yu, Ting Zhai, Qi Xu, Xiaopeng Yang, Jieqiang Wang, Bingqiang Cao**

School of Materials Science and Engineering, Laboratory of Inorganic Energy and Environment Materials, University of Jinan, Jinan 250022, Shandong, PR China

ARTICLE INFO

Article history:
Received 9 January 2017
Received in revised form
14 February 2017
Accepted 20 February 2017
Available online 21 February 2017

Keywords:
TEA sensing property
ZnO morphology
Exposed planes
Atom arrangement

ABSTRACT

Triethylamine (TEA) is one of toxic volatile organic compounds (VOCs) which deserve to be studied in the field of gas sensors. In this paper, three kinds of ZnO samples (microrods, microflowers, and mircropyramids) were synthesized to learn the inner relationship which results in the different TEA sensing performances. Based on the model of surface atoms arrangement and theory of oxygen vacancy, we found that the different surface structures plays crucial role in the TEA sensing properties. Moreover, the order of TEA sensing properties of ZnO crystallite planes is confirmed as list: $(0001) > \{10\bar{1}0\} > \{10\bar{1}1\} > (000\bar{1})$.

1. Introduction

Triethylamine (TEA) is one of a colorless transparent liquid with a strong ammonia-like odor and has been widely used as solvents, catalysts, and raw materials in the process of organic synthesis [1,2]. However, TEA can cause great damage on human health like skin burns, headaches, nausea, eye irritation, and even death due to its combustible and toxicity. According to the regulation of Occupational Safety and Health Administration (OSHA), the concentration of TEA should not exceed the threshold limit of 10 ppm on volumetric basis (ppmV) in air [3–5]. Thus, monitoring TEA and studying its sensing properties is not only meaningful, but also essential.

As a typical n-type metal oxide semiconductor with a wide band gap (3.37 eV) [6–8], ZnO has been applied into many fields, including solar cell [9], photo-catalysts [10], light-emitting diodes [11], lithium storage batteries [12], and so on. In terms of gas sensor, ZnO based sensors have been investigated for a long time due to its desirable characters, such as good morphology controllability, high electron mobility, good chemical stability, and low production cost [13–15]. As for metal oxide semiconductors (MOSs) based gas sensors, the sensing performances are mostly affected by the physical/chemical properties of the crystallite surfaces [16]. Therefore, some works concerning the relationship between planes of crystallite and their corresponding physical/chemical properties have been accomplished [17–30]. Wang and coworkers discovered that the SnO_2 nanoparticles with exposed high-energy planes, such as {221} or {111}, exhibited enhanced catalytic activity for the oxidation of CO [31]. Yang et al. [32] reported a kind of ZnO hexagonal nanodisk networks, which possessed excellent field emission performance. In the field of gas sensing, Han et al. [33] prepared SnO_2 with exposed {221} planes and found those planes have increased gas sensing performance to ethanol compared with the {101} planes. These works have confirmed that the surfaces of crystallite do exhibit different physical/chemical properties. Until now, many works have been carried out to study the gas sensing properties of ZnO by focusing on its various shapes [34,35]. However, to the best of our knowledge, the researches about ZnO based TEA sensors, which learn the relationship between crystal surfaces and sensing properties, are rarely reported. Moreover, different surface atoms arrangement and theory of oxygen vacancy are used to support our analysis.

In this paper, three kinds of typical ZnO microcrystallites

* Corresponding author. School of Materials Science and Engineering, University of Jinan, Jinan 250022, PR China.
** Corresponding author. School of Materials Science and Engineering, University of Jinan, Jinan 250022, PR China.
E-mail addresses: mse_xuhy@ujn.edu.cn (H. Xu), mse_caobq@ujn.edu.cn (B. Cao).

http://dx.doi.org/10.1016/j.jallcom.2017.02.223
0925-8388/

including rods, flowers, and pyramids are synthesized and the corresponding TEA sensing properties were investigated on the same time. The sensing performances of the three kinds of sensors are different due to the different ZnO morphologies. It is found that TEA gas sensor based on ZnO microflowers has not only the highest response but also best selectivity to TEA than others. On the basis of the model of surface atoms arrangement and theory of oxygen vacancy, the effect of ZnO morphologies on the gas sensing mechanism of TEA is analyzed. Moreover, four kinds of dominating ZnO planes with different sensing performance is proposed and ranked.

2. Experimental section

2.1. Synthesis of ZnO crystallites

2.1.1. Synthesis of ZnO rods

ZnO rods were synthesized by a hydro-thermal route. In a typical experiment, 0.66 g $Zn(AC)_2$ $2H_2O$ and 2.4 g NaOH were dissolved in 9 mL deionized water and 21 mL glycerin. The resulting mixture was stirred for several minutes and transferred into a Teflon-lined stainless-steel autoclave with a capacity of about 50 mL. Then the autoclave was heated to 150 °C. After reacting for 24 h, the resulting products were cooled down naturally and washed with deionized water and absolute ethanol for several times to remove the ions possibly remaining in the final products, and finally dried in air at 70 °C.

2.1.2. Synthesis of ZnO flowers

ZnO flowers were also prepared by hydro-thermal process and the steps are described as follows: 0.287 g $ZnSO_4 \cdot 7H_2O$, 0.080 g NaOH, and 0.083 g NaF were added into 7 mL deionized water and 3 mL ethanol. Then the mixture was transferred into 50 mL autoclave after stirring for several minutes. The autoclave was heated at 200 °C for 20 h. The white precipitates were separated by centrifugation and washed thoroughly with deionized water and absolute ethanol. Subsequently, the white precipitates were dried in air at 70 °C.

2.1.3. Synthesis of ZnO pyramids

Molten-salt growth method was used to synthesize ZnO pyramids. Briefly, 0.219 g $Zn(AC)_2$ $2H_2O$ and 6.9 g $LiNO_3$ were mixed together and ground sufficiently. Then the mixture was transferred into Al_2O_3 crucible and heated in the tube furnace for 30 min at 400 °C. After heating, the product was dissolved into deionized water and the precipitate would settle to the bottom of beaker. Then the white precipitates could be collected through washing with deionized water and ethanol and drying at 70 °C in air.

2.2. Material characterizations

The crystallite structure of the products was characterized by X-ray diffraction (XRD, Bruker D8 Advance diffractometer) using CuKal radiation ($\lambda = 0.15406$ nm) at 30 kV and 40 mA at a scanning rate of 2° at 2θ min^{-1} ranging from 10° to 70°. The SEM images of three kinds of samples were recorded on a FEI Sirion 200 field emission gun scanning electron microscope (FESEM, Hitachi S4800). More details about the structure were investigated by high resolution transmission electron microscopy (HRTEM, JEM-2100F, JEOL), energy dispersive X-ray detector (EDX), and the selected area electron diffraction (SEAD) pattern. Besides, the Brunauer–Emmett–Teller (BET) specific surface area of ZnO samples was measured with a N_2 adsorption-desorption analyzer (3W-BK, Beijing).

2.3. Gas sensor fabrication and gas sensing test

In order to increase the crystallization degree, the three kinds of ZnO samples were annealed under 350 °C for 2 h in air. Then the as-prepared ZnO crystallite powder were wetted with appropriate deionized water to form a paste and then coated onto the outside surface of alumina (Al_2O_3) tubes. Fig. 1(a) and (b) are optical photographs of an Al_2O_3 tube and a gas sensor, respectively. A cross-section schematic of the Al_2O_3tube (including a pair of Au electrodes, Pt wires, Alumina tube, Ni-Cr heating coil, and a thick film of sensing materials) is illustrated in Fig. 1(c). Gas sensing properties were tested by a gas-sensing characterization system (WS-30A, Weisheng Electronics Co., Ltd., China) and the photo is shown in Fig. 1(d). Before the measurement, the sensors were aged at 350 °C for 24 h in air.

3. Results and discussion

3.1. Characterization of as-synthesized ZnO samples

First of all, the crystallite structure of three kinds of ZnO samples after annealing was analyzed by XRD. Just as shown in Fig. 2, all the reflection peaks of ZnO samples match well with the diffraction pattern of typical hexagonal wurtzite ZnO structure (JCPDS Card No. 36-1451) and no peaks could be observed for impurities, which

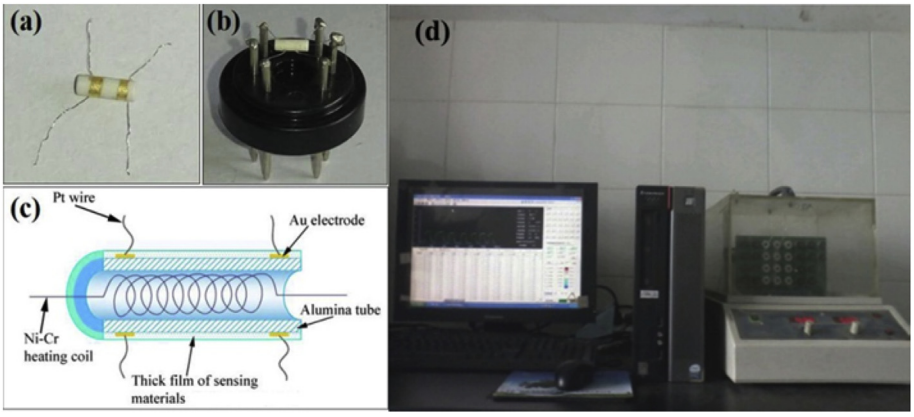

Fig. 1. (a) Gas sensor of ZnO samples fixed on an electronic bracket; (b) Al_2O_3 ceramic tube; (c) Cross-section schematic for the Al_2O_3 ceramic tube covered with ZnO samples; (d) Photo of gas-sensing characterization system.

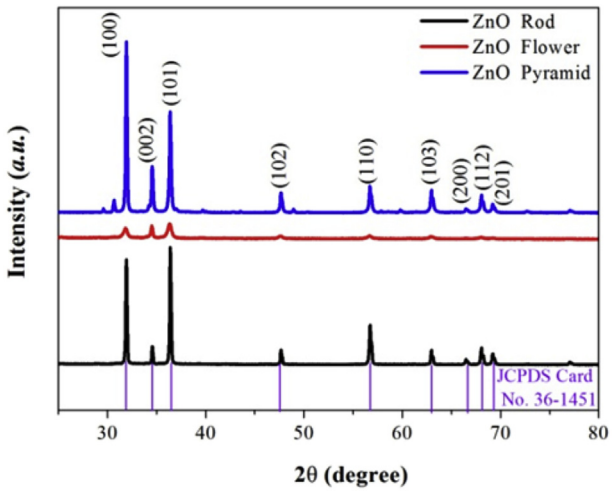

Fig. 2. XRD patterns of three kinds of samples after annealing.

means the samples are pure and have only the wurtzite structure. More information about the ZnO samples is provided in Fig. S1 of the supplementary information. Fig. S1 shows the EDX spectra which illustrates the elemental composition of three kinds of ZnO samples. This result further proves the purity of samples [36–38].

SEM images (Fig. 3) indicate that all of the ZnO crystallites have distinct and regular morphologies in micrometer size. Fig. 3(a) illustrates a rod-shaped structure which are close to a pencil and about 0.6~2 μm in width and 20–40 μm in length. Fig. 3(b) shows the morphology of ZnO flowers assembled by several crystallite flakes. And these crystallite flakes are ~10 nm in thickness and 0.2~1 μm in width. Fig. 3(c) represents the morphology of hexagonal pyramids with 1–3 μm base sizes.

TEM, HRTEM, and SAED characterizations provide us more useful information about the structural details. Fig. 4(a) shows the TEM image of ZnO rod. As can be seen, the synthesized crystallite has a rod like structure with a cusp. The HRTEM image (Fig. 4(b)) represents that ZnO rod has clear lattice fringes with 0.26 nm d-spacing, which corresponding to the distance between two {0001} crystallite planes of wurtzite ZnO. The SAED pattern (Fig. 4(c)) shows a spot pattern which in accordance with the single crystalline wurtzite ZnO structure. The TEM image of ZnO flowers is shown in Fig. 4(d) which indicates that the ZnO flowers are assembled by several flakes with visible surfaces. The HRTEM image (Fig. 4(e)) illustrates that the side surface of the flakes is $\{10\bar{1}0\}$ plane. And the diffraction pattern of ZnO flowers as shown in Fig. 4(f) indicates a polycrystalline structure. Typical TEM image of an individual ZnO pyramid is shown in Fig. 4(g) and its regular hexagonal outline can be seen. As shown in Fig. 4(h), the lattice spacing is 0.247 nm, which represents $\{10\bar{1}1\}$ planes. According to the SAED pattern (Fig. 4(i)) we know that the ZnO pyramid is single crystallite.

The specific surface area of the three kinds of ZnO samples are the most important information in our analysis. Therefore, the BET was performed to estimate the size of specific surface area just as shown in Fig. 5. The result reveals that the specific surface area of ZnO rods, flowers, and pyramids are 37.75, 65.45, and 34.62 m^2/g, with corresponding total pore volume of 0.04, 0.18, and 0.06 cm^3/g, respectively. It can be seen that the specific surface area of ZnO rods and pyramids are similar, which is only about half of that of ZnO flowers. Furthermore, the total pore volume of three kinds of ZnO samples is relatively small, so we consider their surfaces as smooth.

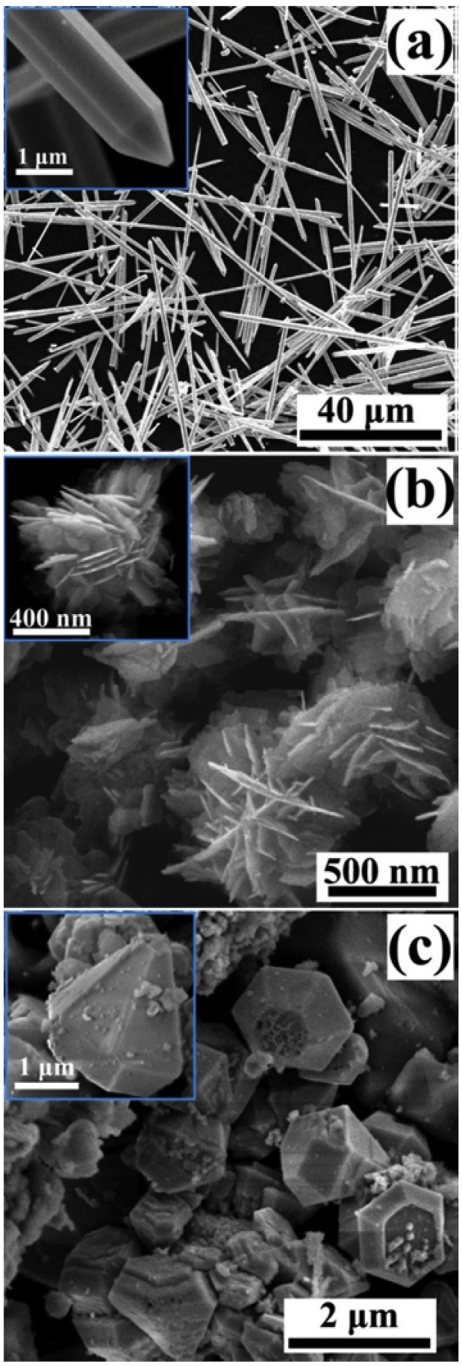

Fig. 3. SEM image of ZnO samples: (a) ZnO rods; (b) ZnO flowers; (c) ZnO pyramids.

3.2. Sensor performance of ZnO samples

Working temperature is the most important factor responsible for the performance of the sensors. Because, the adsorption and desorption are the most primary process for sensing response, which is also influenced by kinetics. And the optimum working temperature is an essential point to keep the balance between kinetics and desorption which are important factors influencing the sensing properties [39,40]. Therefore, the optimum working temperature was evaluated as the first sensing properties. The relationships between the sensing response and the working temperature are shown in Fig. 6. It can be found that the optimum

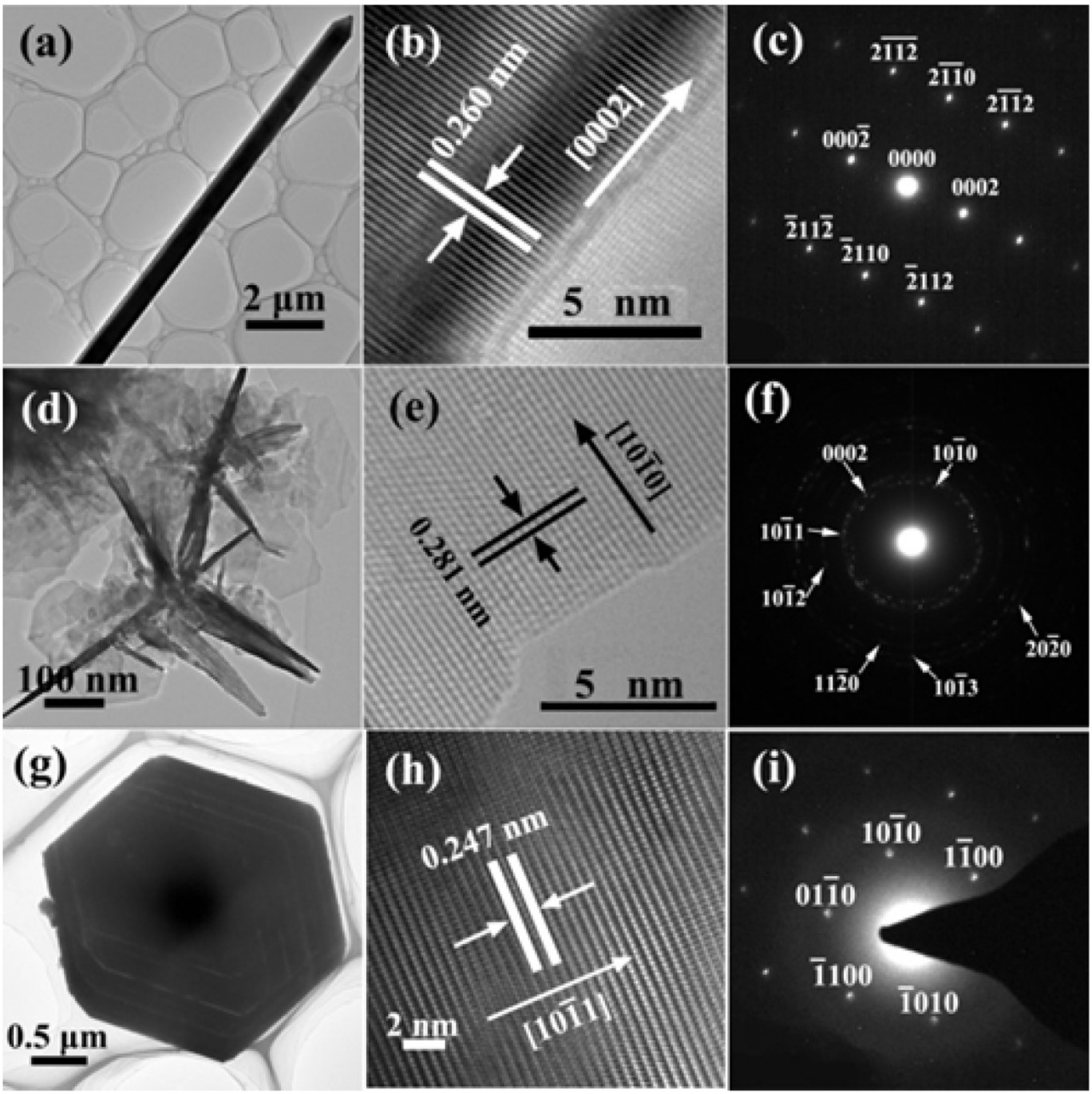

Fig. 4. (a) TEM image, (b) corresponding HRTEM image, and (c) SAED pattern of an individual ZnO rod; (d) TEM image, (e) corresponding HRTEM image, and (f) SAED pattern of an individual ZnO flower; (g) TEM image, (h) corresponding HRTEM image, and (i) SAED pattern of an individual ZnO pyramid.

working temperature of three kinds of samples is 280 °C. Under this temperature, the sensing response of ZnO rods, ZnO flowers, and ZnO pyramids nearly reach 60, 83, and 28, respectively.

Selectivity is also an essential project of gas sensors. Fig. 7 depicts the responses of the three sensors to 50 ppm TEA at 280 °C as well as other gases such as isopropanol, acetone, ethanol, paraxylene, and benzene. It can be observed that the responses to TEA of three kinds of sensors are much higher than that to other gases which indicating their good selectivity for TEA. This phenomenon may be due to the different reaction activity of target gases. The main molecular bond of target gases are C-N (TEA), C-C (isopropanol), O-H (ethanol), C=C (benzene), and C=O (acetone) with the corresponding bond energy are 307, 345, 458.8, 610.3, and 798.9 kJ/mol, respectively [41,42]. Due to the lowest C-N bond energy, TEA molecules are most easy to be detected by ZnO sensors than other gases.

Good repeatability of gas sensors is useful in the real application. Fig. 8 depicts a typical response profile to investigate the repeatability of the three kinds of ZnO sensors. It indicates that all of sensors have good repeatability run after five cycles. Fig. 9(a) shows the response curve of the sensors to TEA of different concentrations from 2 to 500 ppm. With the increasing concentration, the

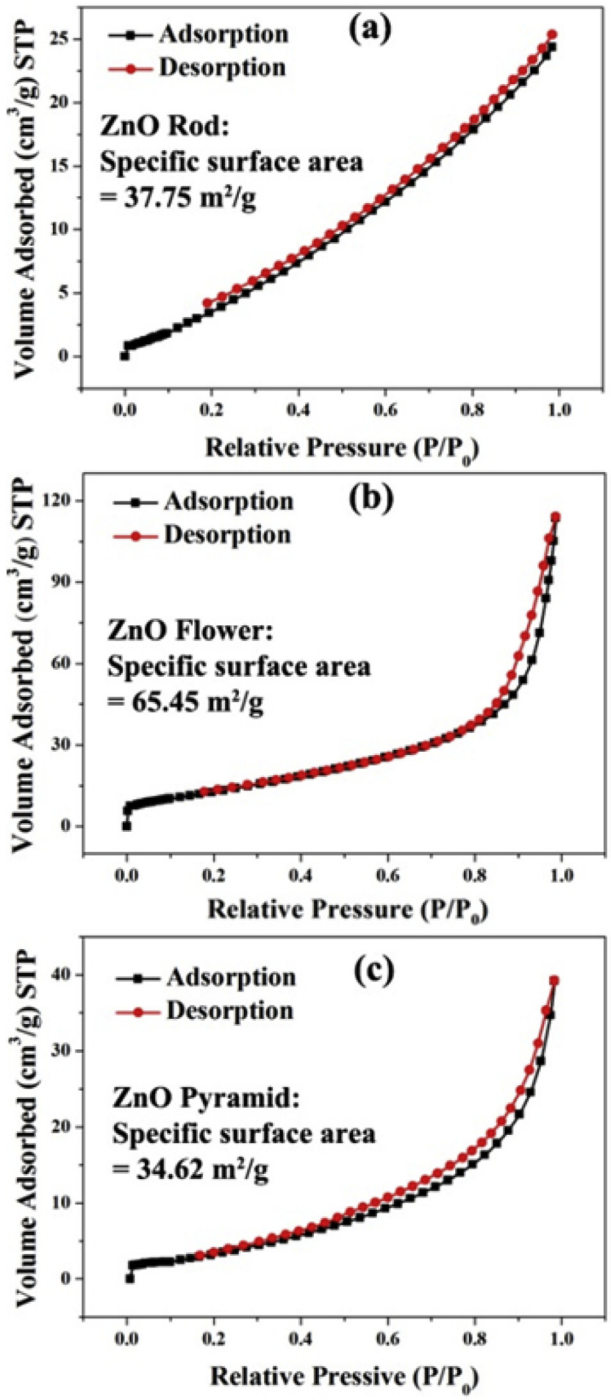

Fig. 5. BET results for ZnO samples: N_2 adsorption-desorption isotherm of (a) ZnO rods, (b) ZnO flowers, and (c) ZnO pyramids.

response curves of the three kinds of sensors raise apparently, which indicated that they have a wide range of detectable concentration. The corresponding relationship between response and concentration is inset in the pattern (a). As for ZnO pyramids, the curve has no obvious rising trend when the concentration exceed 10 ppm. And in our work, the responses exhibit good linear relationship with the concentration in a logarithm scale, as shown in Fig. 9(b). As a whole, ZnO flowers do better than the other two sensors.

The response-recovery time is another important property for

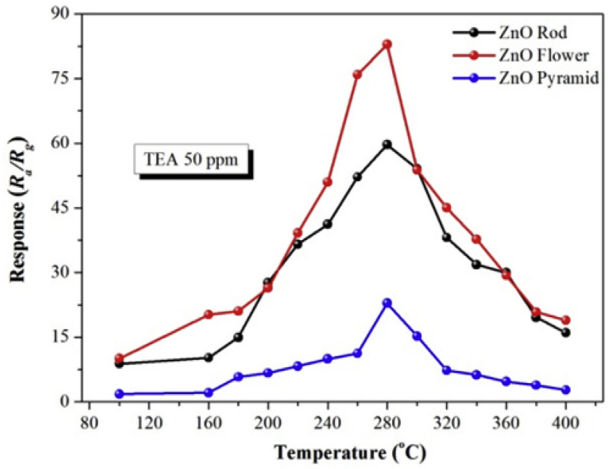

Fig. 6. Curves of gas sensitivity versus working temperature take 50 ppm of TEA as detecting gas.

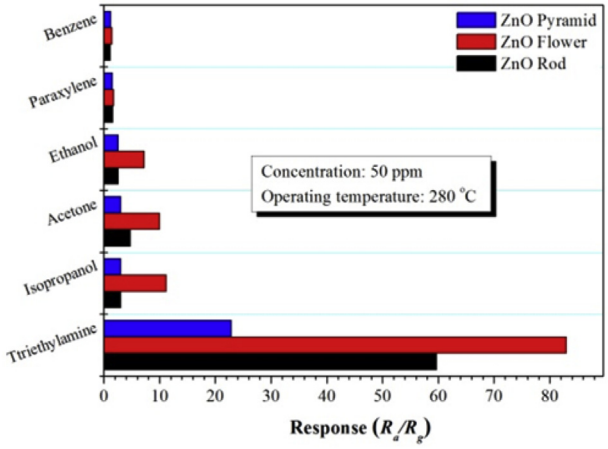

Fig. 7. Selectivity comparison of three sensors for different target gases with the same concentration (50 ppm) at 280 °C.

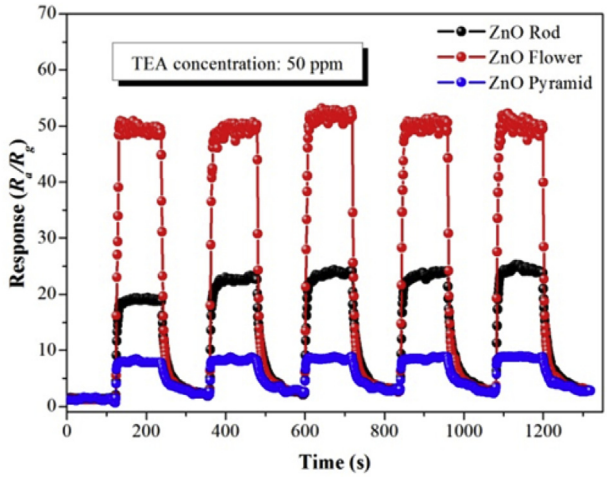

Fig. 8. Repeatability of three sensors to 50 ppm TEA at 280 °C.

gas sensors. The response time (T_{res}) is defined as the time spans to reach a 90% variation in resistance upon exposure to gas, meanwhile, the recovery time (T_{rec}) is fixed as the time necessary for the

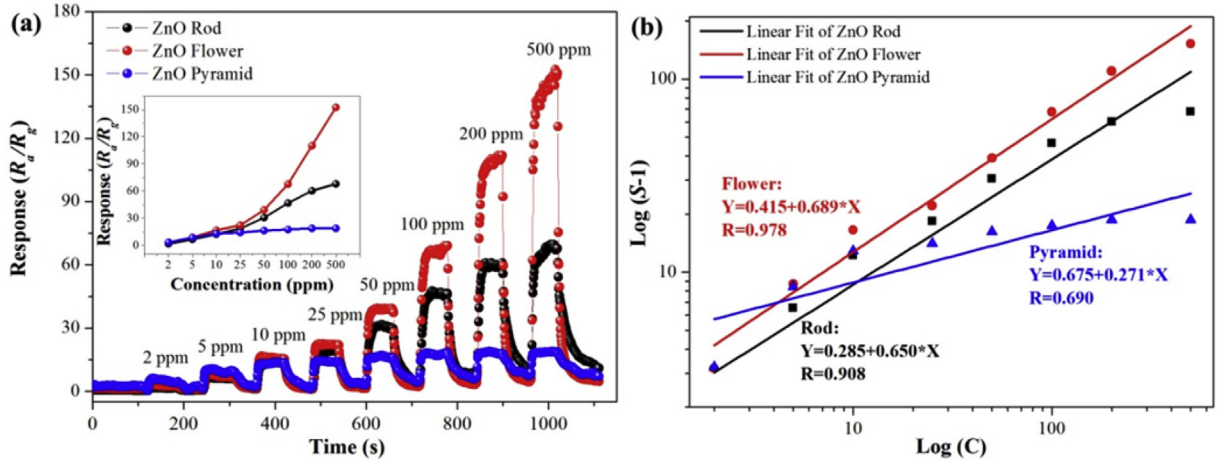

Fig. 9. (a) Responses of three kinds of sensors to TEA of different concentration at 280 °C, (inset pattern) corresponding relationship between response and concentration; (b) the log(*S*-1) versus log(C) plot of three kinds of ZnO sensors for TEA gas and the corresponding linearly fitted results.

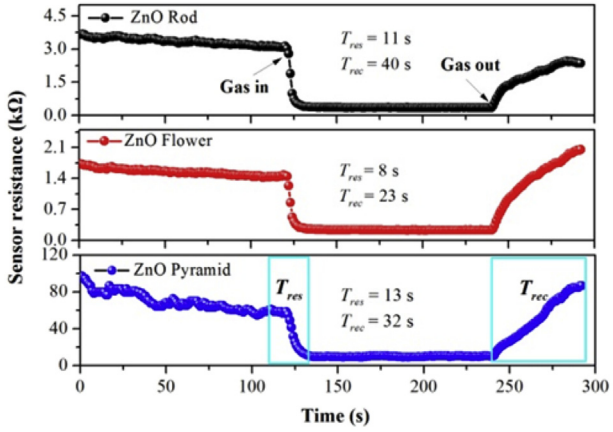

Fig. 10. Response-recovery curves of three sensors to 50 ppm TEA at 280 °C.

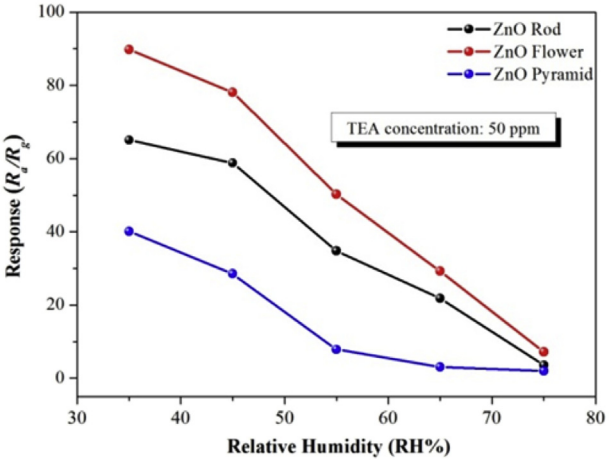

Fig. 11. The relationship between sensing responses and relative humidity (RH%).

sensor to recovery 90% of its initial resistance. In Fig. 10, the T_{res} of three kinds of ZnO samples, including ZnO rods, ZnO flowers, and ZnO pyramids, are 11 s, 8 s, and 13 s, while the T_{rec} are 40 s, 23 s, and 32 s, respectively. Moreover, the research about the relative humidity (RH) is another important project in the field of gas sensors. And in our experiment, the RH has a great impact on the response of the three kinds of sensors. In Fig. 11, the sensing response of three kinds of sensors reduced with the increasing of RH. The main reasons are proposed as follows: Firstly, on the surface of ZnO crystal, the adsorbed water molecules not only reduced the opportunity to form negative oxygen ions, but also make it hard for TEA molecules to move on the surface. So the responses of sensors toward TEA decrease significantly. Secondly, the reaction between the surface oxygen and the water molecules can make a decrease in the sensor baseline resistance and further weaken the response. Thirdly, TEA molecules prefer to react with OH groups of water molecules than adsorbed oxygen. In general, all of these factors result in a decreased sensing response [43–47]. In order to guarantee the same variables, we tested the three kinds of sensors under the same surroundings with a relatively low RH (nearly 35%).

Summering the above sensing performances of three kinds of sensors, it is found that the ZnO flowers sensors exhibit the highest sensing response (83), best selectivity to TEA, and the shortest response/recovery times (8 s/23 s). The ZnO rods sensors have medium sensing response and the ZnO pyramids sensors do the worst. In conclusion, the order of gas sensing properties for the three kinds of ZnO samples can be ranked as followed: flowers > rods > pyramids.

3.3. Explore the relationship between exposed planes of ZnO samples and gas sensing properties

The theory of space-charge layer mode has been widely accepted and applied into the mechanism explanation of the gas sensing [48–50]. Near-surface region of each grain would form charge depletion, due to electron trapping on absorbed oxygen species from surrounding air. As a result, the charge depletion possesses increased resistance. Once the sensor materials exposing to the gas, the gas molecules would reacted with the adsorbed oxygen ions and released the electrons back to the ZnO semiconductor, which leading the resistance decreased. The sensitivity could be calculate by the formula of response ($S = R_a/R_g$). Thus, we know that the absorption of oxygen plays an important role in the progress of sensing response. Moreover, the more oxygen molecules are adsorbed, the higher sensing response would be. Therefore, finding out the relationship between surface properties and oxygen adsorption is the key to explain the different gas sensing

performance of three kinds of ZnO sensors.

It worth noting that, the different atomic arrangement on the surface could affect the adsorption of oxygen molecules [51]. It is well know, the structure of ZnO crystallites can be described as a number of alternating stacked planes with tetrahedrally coordinated O^{2-} and Zn^{2+} ions along the *c*-axis [52,53]. And the intrinsic anisotropy would affect the growth rate of crystallite in various orientations [54–56], which causing the different atomic arrangement on the surface as a result. Normally, in order to lower the high surface energy, the wurtzite type ZnO nanostructures usually tend to expose the nonpolar $\{10\bar{1}0\}$ planes instead of the polar $\{0001\}$ planes in the hydrothermal environment [51]. So, the ZnO crystallites are prefer to grow into rod-like, as what were synthesized in our experiment. In the synthesis experiment of ZnO flowers, F^- was added into the hydrothermal solution to tune the morphology of ZnO, which contributes to the formation of sheet-like ZnO. As the reaction continue, the nanosheets tend to merge together to form ZnO nanoflowers by a self-assembly process. It is possible that the F^- combined with Zn^+ on the $\{0001\}$ planes, which make crystallites extending along $[10\bar{1}0]$ direction [54,57]. Molten salt method was used to synthesize ZnO pyramids. The strong electrostatic interactions would happen between the ions of the molten salt and the polar surfaces of ZnO, which resulting in relatively slow growth rate for the polar planes and forming the pyramid-like ZnO [16].

In order to study the atomic arrangement of the surface in a visible way, we drafted the morphology models of ZnO rod, ZnO flower, and ZnO pyramid in Fig. 12, respectively. The atomic arrangements of the each surface were also simulated on the side. As shown in the picture, four dominating planes are sorted out from the three kinds of ZnO morphologies. The side with blue line represents the surface which is exposed to the air. Observing the picture, the atoms of outermost layers of the Zn-terminated (0001) plane and O-terminated $(000\bar{1})$ plane are Zn^{2+} and O^{2-}, respectively. While the $\{10\bar{1}0\}$ planes composed of equivalent O^{2-} and Zn^{2+} ions at the outermost planes. And the $\{10\bar{1}1\}$ planes are terminated with O^{2-} ions as well. Normally, due to unsaturated oxygen coordination, Zn^{2+} ions are able to seize atmosphere oxygen (O_2) through physical/chemical absorption to achieving energy balance on the structure. While the terminated O^{2-} ions are impossible to further absorb oxygen molecules or other oxygen species [32]. According to the above analyze, the sensing activity of

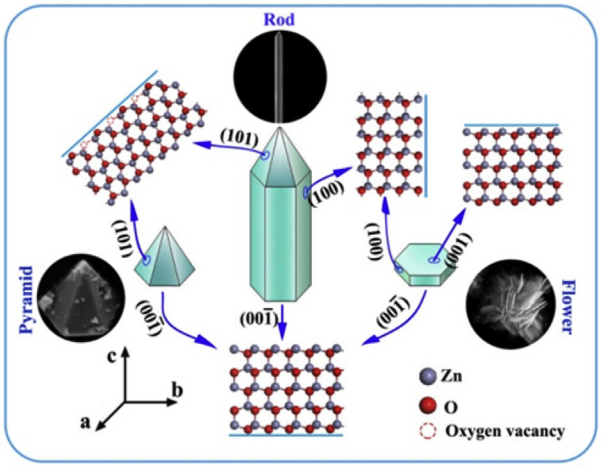

Fig. 12. Schematic illustration of the morphology models for ZnO rods, ZnO flowers, and ZnO pyramids; and atomic stacking model of different wurtzite ZnO planes: (0001), $\{10\bar{1}0\}$, $\{10\bar{1}1\}$, and $(000\bar{1})$.

Table 1
The important information comparison of three kinds of ZnO crystallites.

Morphology of ZnO	BET (m^2/g)	Sensing response	Dominating planes
Flower	65.45	83	(0001)
Rod	37.75	60	$\{10\bar{1}0\}$
Pyramid	34.62	28	$\{10\bar{1}1\}$

the ZnO planes could be sorted in this order: $(0001) > \{10\bar{1}0\} > (000\bar{1})$ and $\{10\bar{1}1\}$.

This hypothesis could be confirmed by the result of the sensing measure. Combining with the information of SEM (Fig. 3), BET (Fig. 5), and morphology models (Fig. 12), the surface condition of three kinds of ZnO crystallites are deeply discussed as follows. Firstly, towards ZnO flowers, the dominating plane with gas sensing response is (0001) plane. There are two main reasons: on the one hand, $(000\bar{1})$ plane almost has no response to gases due to the termination of oxygen; on the other hand, $\{10\bar{1}0\}$ planes (side surface) are low-energy planes and have little contribution to gas sensing response because the flake is quite thin. Secondly, as for ZnO rods, the dominating planes are six $\{10\bar{1}0\}$ planes. Because, learning form the result of SEM, every single rod is more than 40 μm in length while only 1 μm in radius. Therefore, the six $\{10\bar{1}1\}$ planes (top surfaces) and one $(000\bar{1})$ plane (bottom surfaces) occupies a very small proportion of the whole surface, which have few influence in the sensing response. Similarly, the six $\{10\bar{1}1\}$ planes (side surfaces) are the dominating planes for ZnO pyramids. In addition, specific surface area of materials is another important factor, which can't be ignored. Just as illustrated by Fig. 5, the specific surface area of ZnO flowers (65.45 m^2/g) are nearly twice times than that of ZnO rods (37.75 m^2/g) and ZnO pyramids (34.62 m^2/g). Moreover, the area of (0001) plane (top surface) only possess a half of the whole flower, which is close to the whole surface area of ZnO rods and ZnO pyramids. For this reason, these three dominating planes are supposed to exhibit the similar specific surface area. In order to understand the relationship between the three kinds of ZnO, the important information of three kinds of ZnO crystallites including BET results, sensing response, and dominating planes are concluded in Table 1. Combining with Table 1, it can be got that the order of sensing ability of three dominating planes could be listed as: $(0001) > \{10\bar{1}0\} > \{10\bar{1}1\}$.

Till now, we haven't found direct method to compare gas sensing activity of $\{10\bar{1}1\}$ plane with that of $(000\bar{1})$ plane. But there are several reports discussed the properties of $\{10\bar{1}1\}$ plane and $(000\bar{1})$ plane. For example, Jiang et al. [58] reported that the $\{10\bar{1}1\}$ plane of ZnO has more oxygen vacancies than the $(000\bar{1})$ plane, because there are many surplus charges existed on the $\{10\bar{1}1\}$ plane. And the presence of the oxygen vacancies could enhance gas sensing of ZnO based sensors [38,59,60]. So the gas sensing activity of $\{10\bar{1}1\}$ plane is stronger than that of $(000\bar{1})$ plane. In summary, the final order of the gas sensing activity could be proposed as follows: $(0001) > \{10\bar{1}0\} > \{10\bar{1}1\} > (000\bar{1})$, which agrees well with our experimental results of gas sensing properties.

4. Conclusions

In this work, ZnO microrods, ZnO microflowers, and ZnO micropyramids was synthesized, respectively. And it was observed that the gas sensing performances are different among the different morphologies of ZnO crystallites. Furthermore, the relationship between planes of ZnO and gas sensing properties was studied. On the basis of experiment and some related references, it was founded that the sensing response would rise with the increase of adsorbed oxygen, and the exposed Zn^{2+} ions can absorb oxygen

molecules while the exposed O^{2-} ions can't. This should be the main reason for the differences in their gas sensing performances. In summary, the order of gas sensing properties of ZnO planes was proposed: $(0001) > \{10\bar{1}0\} > \{10\bar{1}1\} > (000\bar{1})$. The study should be helpful for improving the gas sensing properties of metal oxides from the angle of anisotropy of crystallites.

Acknowledgments

This work is supported by National Natural Science Foundation of China (NSFC, No. 60906008), Shan-dong Provincial Science Foundation (No. ZR2014JL045 and ZR2015BQ006) and Science Foundation of University of Jinan (No. XKY1504).

Appendix A. Supplementary data

Supplementary data related to this article can be found at http://dx.doi.org/10.1016/j.jallcom.2017.02.223.

References

[1] Y.Z. Lv, C.R. Li, L. Guo, F.C. Wang, Y. Xu, X.F. Chu, Triethylamine gas sensor based on ZnO nanorods prepared by a simple solution route, Sens. Actuators B 141 (2009) 85–88.
[2] H.Y. Xu, D.X. Ju, W.R. Li, J. Zhang, J.Q. Wang, B.Q. Cao, Superior triethylamine-sensing properties based on TiO_2/SnO_2 n-n heterojunction nanosheets directly grown on ceramic tubes, Sens. Actuators B 228 (2016) 634–642.
[3] L. Xu, H.J. Song, J. Hu, Y. Lv, K.L. Xu, A cataluminescence gas sensor for triethylamine based on nanosized LaF_3-CeO_2, Sens. Actuators B 169 (2012) 261–266.
[4] D.X. Ju, H.Y. Xu, Q. Xu, H.B. Gong, Z.W. Qiu, J. Guo, J. Zhang, B.Q. Cao, High triethylamine-sensing properties of NiO/SnO_2 hollow sphere P-N heterojunction sensors, Sens. Actuators B 215 (2015) 39–44.
[5] B. Gandu, K. Sandhya, A.G. Rao, Y.V. Swamy, Gas phase bio filter for the removal of triethylamine (TEA) from air: microbial diversity analysis with reference to design parameters, Bioresour. Technol. 139 (2013) 155–160.
[6] L.X. Zhang, J.H. Zhao, H.Q. Lu, L. Li, J.F. Zheng, J. Zhang, H. Li, Z.P. Zhu, Highly sensitive and selective dimethylamine sensors based on hierarchical ZnO architectures composed of nanorods and nanosheet-assembled microspheres, Sens. Actuators B 171–172 (2012) 1101–1109.
[7] X.H. Liu, J. Zhang, L.W. Wang, T.L. Yang, X.Z. Guo, S.H. Wu, S.R. Wang, 3D hierarchically porous ZnO structures and their functionalization by Au nanoparticles for gas sensors, J. Mater. Chem. A 21 (2011) 349–356.
[8] Z.P. Fu, Z. Wang, B.F. Yang, Y.L. Yang, H.W. Yan, L.S. Xia, Shape-control of nano ZnO by changing the solvent, Mater. Lett. 61 (2007) 4832–4835.
[9] S.B. Zhu, X. Tian, J.J. Chen, L.M. Shan, X.L. Xu, Z.W. Zhou, A facile approach to construct multiple structured ZnO crystals by trisodium citrate-assisted hydrothermal growth toward performance enhancement of dye-sensitized solar cells, J. Phys. Chem. C 118 (2014) 16401–16407.
[10] T.K. Nguyen, W.K. Soon, H.Y. Dae, C. Shinuk, J.K. Eui, H.H. Sung, Fabrication of Au/graphene-wrapped ZnO-nanoparticle-assembled hollow spheres with effective photoinduced charge transfer for photocatalysis, ACS Appl. Mater. Interfaces 7 (2015) 3524–3531.
[11] S.C. Li, K. Yu, Y. Wang, Z.L. Zhang, C.Q. Song, H.H. Yin, Q. Ren, Z.Q. Zhu, Cu_2S@ZnO hetero-nanostructures: facile synthesis, morphology-evolution and enhanced photocatalysis and field emission properties, CrystEngComm 15 (2013) 1753–1761.
[12] C.Q. Zhang, J.P. Tu, X.H. Huang, Y.F. Yuan, X.T. Chen, F. Mao, Preparation and electrochemical performances of cubic shape Cu_2O as anode material for lithium ion batteries, J. Alloys Compd. 441 (2007) 52–56.
[13] I.S. Hwang, S.J. Kim, J.K. Choi, J. Choi, H. Ji, G.T. Kim, G. Cao, J.H. Lee, Synthesis and gas sensing characteristics of highly crystalline ZnO-SnO_2 core-shell nanowires, Sens. Actuators B Chem. 148 (2010) 595–600.
[14] K.W. Kim, P.S. Cho, S.J. Kim, J.H. Lee, C.Y. Kang, J.S. Kim, S.J. Yoon, The selective detection of C_2H_5OH using SnO_2-ZnO thin film gas sensors prepared by combinatorial solution deposition, Sens. Actuators B 123 (2007) 318–324.
[15] Z. Qin, Y.H. Huang, J.J. Qi, H. Feng, L.J. Su, Y. Zhang, Facile synthesis and photoelectro chemical performance of the bush-like ZnO nanosheets film, Solid State Sci. 14 (2012) 155–158.
[16] T. Xu, X. Zhou, Z.Y. Jiang, Q. Kuang, Z.X. Xie, L.S. Zheng, Syntheses of nano/submicrostructured metal oxides with all polar surfaces exposed via a molten salt route, Cryst. Growth & Des. 9 (2009) 192–196.
[17] K.B. Rider, K.S. Hwang, M. Salmeron, G.A. Somorjai, High-pressure (1Torr) scanning tunneling microscopy (STM) study of the coadsorption and exchange of CO and NO on the Rh (111) crystal face, J. Am. Chem. Soc. 124 (2002) 5588–5593.
[18] V. Rosca, G.L. Beltramo, M.T. Koper, Reduction of NO adlayers on Pt (110) and Pt (111) in acidic media: evidence for adsorption site-specific reduction, Langmuir 21 (2005) 1448–1456.
[19] A. Tillekaratne, D. Siap, M. Trenary, Adsorption and dehydrogenation of ortho-carborane on the Pt (111) surface, J. Phys. Chem. C 112 (2008) 8682–8689.
[20] Y. Ikezawa, R. Masuda, Adsorption behavior of terephthalic acid on Au (100), Au (111) and Au (110) electrodes in neutral solution, ElectrochimicaActa 53 (2008) 5456–5463.
[21] A.D. Smeltz, R.B. Getman, W.F. Schneider, F.H. Ribeiro, Coupled theoretical and experimental analysis of surface coverage effects in Pt-catalyzed NO and O_2 reaction to NO_2 on Pt (111), Catal. Today 136 (2008) 84–92.
[22] S. Pick, Density-functional study of the CO adsorption on ferromagnetic Co (0001) and Co (111) surfaces, Surf. Sci. 601 (2007) 5571–5575.
[23] M.J.S. Spencer, N. Todorova, I. Yarovsky, H_2S dissociation on the Fe (100) surface: an ab initio molecular dynamics study, Surf. Sci. 602 (2008) 1547–1553.
[24] J.M. Jin, W.F. Lin, P.A. Christensen, The effects of the specific adsorption of anion on the reactivity of the Ru (0001) surface towards CO adsorption and oxidation: in situ FTIRS studies, Phys. Chem. Chem. Phys. 10 (2008) 3774–3783.
[25] M.J. Herbich, M. Milkowska, R. Slojkowska, Adsorption of 1-butanol and 2-butanol on Ag (100) and Ag (110) surfaces, Colloids Surf. A Physicochem. Eng. Asp. 197 (2002) 235–243.
[26] J. Yoshihara, J.M. Campbell, C.T. Campbell, Cu films on a Zn-terminated ZnO (0001) surface: structure and electronic properties, Surf. Sci. 406 (1998) 235–245.
[27] R. Hengerer, B. Bolliger, X.M. Bolliger, M. Gratzel, Structure and stability of the anatase TiO_2 (101) and (001) surfaces, Surf. Sci. 460 (2000) 162–169.
[28] J. Scaranto, S.J. Giorgianni, A quantum-mechanical study of CO adsorbed on TiO_2: a comparison of the Lewis acidity of the rutile (110) and the anatase (101) surfaces, J. Mol. Struct. Theochem. 858 (2008) 72–76.
[29] S.C. Petitto, E.M. Marsh, G.A. Carson, M.A. Langell, Cobalt oxide surface chemistry: the interaction of CoO (100), Co_3O_4 (110) and Co_3O_4 (111) with oxygen and water, J. Mol. Catal. A Chem. 281 (2008) 49–58.
[30] Q. Kuang, X. Wang, Z.Y. Jiang, Z.X. Xie, L.S. Zheng, High-energy-surface engineered metal oxide micro- and nanocrystallites and their applications, Acc. Chem. Res. 47 (2014) 308–318.
[31] X. Wang, X.G. Han, S.F. Xie, Q. Kuang, Y.Q. Jiang, S.B. Zhang, X.L. Mu, X.G. Chen, Z.X. Xie, L.S. Zheng, Controlled synthesis and enhanced catalytic and gas-sensing properties of tin dioxide nanoparticles with exposed high-energy facets, Chem. Eur. J. 18 (2012) 2283–2289.
[32] F. Yang, W.H. Liu, X.W. Wang, J. Zheng, R.Y. Shi, H. Zhao, H.Q. Yang, Controllable low temperature vapor-solid growth and hexagonal disk enhanced field emission property of ZnO nanorod arrays and hexagonal nanodisk networks, ACS Appl. Mater. Interfaces 4 (2012) 3852–3859.
[33] X.G. Han, M.S. Jin, S.F. Xie, Q. Kuang, Z.Y. Jiang, Y.Q. Jiang, Z.X. Xie, L.S. Zheng, Synthesis of tin dioxide octahedral nanoparticles with exposed high-energy {221} facets and enhanced gas-sensing properties, Angew. Chem. Int. Ed. 48 (2009) 9180–9183.
[34] J.B. Cui, L.Q. Shi, T.F. Xie, D.J. Wang, Y.H. Lin, UV-light illumination room temperature HCHO gas-sensing mechanism of ZnO with different nanostructures, Sens. Actuators B 227 (2016) 220–226.
[35] J. Jońca, A. Ryzhikov, M.L. Kahn, K. Fajerwerg, B. Chaudretc, A. Chapelled, P. Meninid, P. Fau, Shape-controlled ZnO nanostructures for gas sensing applications, Procedia Eng. 87 (2014) 907–910.
[36] W. Raza, M.M. Haque, M. Muneer, Synthesis of visible light driven ZnO: characterization and photocatalytic performance, Appl. Surf. Sci. 322 (2014) 215–224.
[37] R.M. Tripathi, A.S. Bhadwal, R.K. Gupta, P. Singh, A. Shrivastav, B.R. Shrivastav, ZnO nanoflowers: novel biogenic synthesis and enhanced photocatalytic activity, J. Photochem. Photobiol. B Biol. 141 (2014) 288–295.
[38] D.E. Motaung, G.H. Mhlongo, I. Kortidis, S.S. Nkosi, G.F. Malgas, B.W. Mwakikunga, S.S. Ray, G. Kiriakidis, Structural and optical properties of ZnO nanostructures grown by aerosol spray pyrolysis: candidates for room temperature methane and hydrogen gas sensing, Appl. Surf. Sci. 279 (2013) 142–149.
[39] A. Kolmakov, D.O. Klenov, Y. Lilach, S. Stemmer, M. Moskovits, Enhanced gas sensing by individual SnO_2 nanowires and nanobelts functionalized with Pd catalyst particles, Nano Lett. 5 (2005) 667–673.
[40] R. Jain, Y. Lei, R. Maric, Ultra-low NO_2 detection by gamma WO_3 synthesized by reactive spray deposition technology, Sens. Actuators B 236 (2016) 163–172.
[41] D.X. Ju, H.Y. Xu, Z.W. Qiu, Z.C. Zhang, Q. Xu, J. Zhang, J.Q. Wang, B.Q. Cao, Near room temperature, fast-response, and highly sensitive Triethylamine sensor assembled with Au-loaded ZnO/SnO_2 core-shell nanorods on flat alumina substrates, ACS Appl. Mater. Interfaces 7 (2015) 19163–19171.
[42] D.X. Ju, H.Y. Xu, Z.W. Qiu, J. Guo, J. Zhang, B.Q. Cao, Highly sensitive and selective TEA-sensing properties of nanosheets directly grown on ceramic tube by forming NiO/ZnO PN heterojunction, Sens. Actuators B 200 (2014) 288–296.
[43] H.S. Hong, G.S. Chung, Controllable growth of oriented ZnO nanorods using Ga-Doped seed layers and surface acoustic wave humidity sensor, Sens. Actuators B 195 (2014) 446–451.
[44] E.X. Chen, H.Y. Yang, J. Zhang, Zeolitic imidazolate framework as formaldehyde gas sensor, Inorg. Chem. 53 (2014) 5411–5413.
[45] S.H. Park, J.Y. Ryu, H.H. Choi, T.H. Kwon, Zinc oxide thin film doped with Al_2O_3, TiO_2 and V_2O_5 as sensitive sensor for trimethylamine gas, Sens. Actuators B 46 (1998) 75–79.

[46] J. Gong, Q. Chen, M. Lian, N. Liu, R.G. Stevenson, F. Adamic, Micromachined nanocrystalline silver doped SnO_2 H_2S sensor, Sens. Actuators B 114 (2006) 32–39.
[47] N. Barsan, U. Weimar, Understanding the fundamental principles of metal oxide based gas sensors the example of CO sensing with SnO_2 sensors in the presence of humidity, J. Phys. Condens. Matter 15 (2003) 813–839.
[48] D.X. Ju, H.Y. Xu, J. Zhang, J. Guo, B.Q. Cao, Direct hydrothermal growth of ZnO nanosheets on electrode for ethanol sensing, Sens. Actuators B 201 (2014) 444–451.
[49] Z.J. Wang, Z.Y. Li, J.H. Sun, H.N. Zhang, W. Wang, W. Zheng, C. Wang, Improved hydrogen monitoring properties based on p-NiO/n-SnO_2 heterojunction composite nanofibers, J. Phys. Chem. C 114 (2010) 6100–6105.
[50] A. Kolmakov, Y. Zhang, G. Cheng, M. Moskovits, Detection of CO and CO_2 using tin oxide nanowire sensors, Adv. Mater. 15 (2003) 997–1000.
[51] X.G. Han, H.Z. He, Q. Kuang, X. Zhou, X.H. Zhang, T. Xu, Z.X. Xie, L.S. Zheng, Controlling morphologies and tuning the related properties of nano/micro-structured ZnO crystallites, J. Phys. Chem. C 113 (2009) 584–589.
[52] B. Meyer, D. Marx, Density-Functional study of the structure and stability of ZnO surface, Phys. Rev. B Condens. Matter 67 (2003) 039902.
[53] Z.H. Jing, J.H. Zhan, Fabrication and gas-sensing properties of porous ZnO nanoplates, Adv. Mater. 20 (2008) 4547–4551.
[54] E.S. Jang, J.H. Won, S.J. Hwang, J.H. Choy, Fine tuning of the face orientation of ZnO crystals to optimize their photocatalytic activity, Adv. Mater. 18 (2006) 3309–3312.
[55] W.J. Li, E.W. Shi, W.Z. Zhong, Z.W. Yin, Growth mechanism and growth habit of oxide crystals, J. Cryst. Growth 203 (1999) 186–196.
[56] J.H. Choy, E.S. Jang, J.H. Won, J.H. Chung, D.J. Jang, Y.W. Kim, Soft solution route to directionally grown ZnO nanorod arrays on Si wafer room-temperature ultraviolet laser, Adv. Mater. 15 (2003) 1911–1914.
[57] L.H. Xue, X.T. Mei, W.X. Zhang, L.X. Yuan, X.L. Hu, Y.H. Huang, K. Yanagisawa, Synthesis and assembly of zinc hydroxide sulfate large flakes: application in gas sensor based on a novel surface mount technology, Sens. Actuators B 147 (2010) 495–501.
[58] Z.Y. Jiang, Q. Kuang, Z.X. Xie, L.S. Zheng, Syntheses and properties of micro/nanostructured crystallites with high-energy surfaces, Adv. Funct. Mater. 20 (2010) 3634–3645.
[59] W. Kim, M. Choi, K. Yong, Generation of oxygen vacancies in ZnO nanorods/films and their effects on gas sensing properties, Sens. Actuators B 209 (2015) 989–996.
[60] L.W. Wang, Y.F. Kang, X.H. Liu, S.M. Zhang, W.P. Huang, S.R. Wang, ZnO nanorod gas sensor for ethanol detection, Sens. Actuators B 162 (2012) 237–243.